Fermilab FERMILAB-PUB-04-207-E CDF SEPTEMBER 2004

Measurement of the $t\bar{t}$ Production Cross Section in $p\bar{p}$ Collisions at $\sqrt{s} = 1.96$ TeV Using Kinematic Fitting of b-tagged Lepton+Jet Events

D. Acosta,[16] J. Adelman,[12] T. Affolder,[9] T. Akimoto,[54] M.G. Albrow,[15] D. Ambrose,[43] S. Amerio,[42] D. Amidei,[33] A. Anastassov,[50] K. Anikeev,[31] A. Annovi,[44] J. Antos,[1] M. Aoki,[54] G. Apollinari,[15] T. Arisawa,[56] J-F. Arguin,[32] A. Artikov,[13] W. Ashmanskas,[15] A. Attal,[7] F. Azfar,[41] P. Azzi-Bacchetta,[42] N. Bacchetta,[42] H. Bachacou,[28] W. Badgett,[15] A. Barbaro-Galtieri,[28] G.J. Barker,[25] V.E. Barnes,[46] B.A. Barnett,[24] S. Baroiant,[6] M. Barone,[17] G. Bauer,[31] F. Bedeschi,[44] S. Behari,[24] S. Belforte,[53] G. Bellettini,[44] J. Bellinger,[58] E. Ben-Haim,[15] D. Benjamin,[14] A. Beretvas,[15] A. Bhatti,[48] M. Binkley,[15] D. Bisello,[42] M. Bishai,[15] R.E. Blair,[2] C. Blocker,[5] K. Bloom,[33] B. Blumenfeld,[24] A. Bocci,[48] A. Bodek,[47] G. Bolla,[46] A. Bolshov,[31] P.S.L. Booth,[29] D. Bortoletto,[46] J. Boudreau,[45] S. Bourov,[15] C. Bromberg,[34] E. Brubaker,[12] J. Budagov,[13] H.S. Budd,[47] K. Burkett,[15] G. Busetto,[42] P. Bussey,[19] K.L. Byrum,[2] S. Cabrera,[14] P. Calafiura,[28] M. Campanelli,[18] M. Campbell,[33] A. Canepa,[46] M. Casarsa,[53] D. Carlsmith,[58] S. Carron,[14] R. Carosi,[44] M. Cavalli-Sforza,[3] A. Castro,[4] P. Catastini,[44] D. Cauz,[53] A. Cerri,[28] C. Cerri,[44] L. Cerrito,[23] J. Chapman,[33] C. Chen,[43] Y.C. Chen,[1] M. Chertok,[6] G. Chiarelli,[44] G. Chlachidze,[13] F. Chlebana,[15] I. Cho,[27] K. Cho,[27] D. Chokheli,[13] M.L. Chu,[1] S. Chuang,[58] J.Y. Chung,[38] W-H. Chung,[58] Y.S. Chung,[47] C.I. Ciobanu,[23] M.A. Ciocci,[44] A.G. Clark,[18] D. Clark,[5] M. Coca,[47] A. Connolly,[28] M. Convery,[48] J. Conway,[6] B. Cooper,[30] M. Cordelli,[17] G. Cortiana,[42] J. Cranshaw,[52] J. Cuevas,[10] R. Culbertson,[15] C. Currat,[28] D. Cyr,[58] D. Dagenhart,[5] S. Da Ronco,[42] S. D'Auria,[19] P. de Barbaro,[47] S. De Cecco,[49] G. De Lentdecker,[47] S. Dell'Agnello,[17] M. Dell'Orso,[44] S. Demers,[47] L. Demortier,[48] M. Deninno,[4] D. De Pedis,[49] P.F. Derwent,[15] C. Dionisi,[49] J.R. Dittmann,[15] P. Doksus,[23] A. Dominguez,[28] S. Donati,[44] M. Donega,[18] J. Donini,[42] M. D'Onofrio,[18] T. Dorigo,[42] V. Drollinger,[36] K. Ebina,[56] N. Eddy,[23] R. Ely,[28] R. Erbacher,[6] M. Erdmann,[25] D. Errede,[23] S. Errede,[23] R. Eusebi,[47] H-C. Fang,[28] S. Farrington,[29] I. Fedorko,[44] R.G. Feild,[59] M. Feindt,[25] J.P. Fernandez,[46] C. Ferretti,[33] R.D. Field,[16] I. Fiori,[44] G. Flanagan,[34] B. Flaugher,[15] L.R. Flores-Castillo,[45] A. Foland,[20] S. Forrester,[6] G.W. Foster,[15] M. Franklin,[20] J. Freeman,[28] H. Frisch,[12] Y. Fujii,[26] I. Furic,[12] A. Gajjar,[29] A. Gallas,[37] J. Galyardt,[11] M. Gallinaro,[48] M. Garcia-Sciveres,[28] A.F. Garfinkel,[46] C. Gay,[59] H. Gerberich,[14] D.W. Gerdes,[33] E. Gerchtein,[11] S. Giagu,[49] P. Giannetti,[44] A. Gibson,[28] K. Gibson,[11] C. Ginsburg,[58] K. Giolo,[46] M. Giordani,[53] G. Giurgiu,[11] V. Glagolev,[13] D. Glenzinski,[15] M. Gold,[36] N. Goldschmidt,[33] D. Goldstein,[7] J. Goldstein,[41] G. Gomez,[10] G. Gomez-Ceballos,[31] M. Goncharov,[51] O. González,[46] I. Gorelov,[36] A.T. Goshaw,[14] Y. Gotra,[45] K. Goulianos,[48] A. Gresele,[4] M. Griffiths,[29] C. Grosso-Pilcher,[12] M. Guenther,[46] J. Guimaraes da Costa,[20] C. Haber,[28] K. Hahn,[43] S.R. Hahn,[15] E. Halkiadakis,[47] A. Hamilton,[32] R. Handler,[58] F. Happacher,[17] K. Hara,[54] M. Hare,[55] R.F. Harr,[57] R.M. Harris,[15] F. Hartmann,[25] K. Hatakeyama,[48] J. Hauser,[7] C. Hays,[14] H. Hayward,[29] E. Heider,[55] B. Heinemann,[29] J. Heinrich,[43] M. Hennecke,[25] M. Herndon,[24] C. Hill,[9] D. Hirschbuehl,[25] A. Hocker,[47] K.D. Hoffman,[12] A. Holloway,[20] S. Hou,[1] M.A. Houlden,[29] B.T. Huffman,[41] Y. Huang,[14] R.E. Hughes,[38] J. Huston,[34] K. Ikado,[56] J. Incandela,[9] G. Introzzi,[44] M. Iori,[49] Y. Ishizawa,[54] C. Issever,[9]

A. Ivanov,[47] Y. Iwata,[22] B. Iyutin,[31] E. James,[15] D. Jang,[50] J. Jarrell,[36] D. Jeans,[49] H. Jensen,[15] E.J. Jeon,[27] M. Jones,[46] K.K. Joo,[27] S. Jun,[11] T. Junk,[23] T. Kamon,[51] J. Kang,[33] M. Karagoz Unel,[37] P.E. Karchin,[57] S. Kartal,[15] Y. Kato,[40] Y. Kemp,[25] R. Kephart,[15] U. Kerzel,[25] V. Khotilovich,[51] B. Kilminster,[38] D.H. Kim,[27] H.S. Kim,[23] J.E. Kim,[27] M.J. Kim,[11] M.S. Kim,[27] S.B. Kim,[27] S.H. Kim,[54] T.H. Kim,[31] Y.K. Kim,[12] B.T. King,[29] M. Kirby,[14] L. Kirsch,[5] S. Klimenko,[16] B. Knuteson,[31] B.R. Ko,[14] H. Kobayashi,[54] P. Koehn,[38] D.J. Kong,[27] K. Kondo,[56] J. Konigsberg,[16] K. Kordas,[32] A. Korn,[31] A. Korytov,[16] K. Kotelnikov,[35] A.V. Kotwal,[14] A. Kovalev,[43] J. Kraus,[23] I. Kravchenko,[31] A. Kreymer,[15] J. Kroll,[43] M. Kruse,[14] V. Krutelyov,[51] S.E. Kuhlmann,[2] N. Kuznetsova,[15] A.T. Laasanen,[46] S. Lai,[32] S. Lami,[48] S. Lammel,[15] J. Lancaster,[14] M. Lancaster,[30] R. Lander,[6] K. Lannon,[38] A. Lath,[50] G. Latino,[36] R. Lauhakangas,[21] I. Lazzizzera,[42] Y. Le,[24] C. Lecci,[25] T. LeCompte,[2] J. Lee,[27] J. Lee,[47] S.W. Lee,[51] R. Lefevre,[3] N. Leonardo,[31] S. Leone,[44] J.D. Lewis,[15] K. Li,[59] C. Lin,[59] C.S. Lin,[15] M. Lindgren,[15] T.M. Liss,[23] D.O. Litvintsev,[15] T. Liu,[15] Y. Liu,[18] N.S. Lockyer,[43] A. Loginov,[35] M. Loreti,[42] P. Loverre,[49] R-S. Lu,[1] D. Lucchesi,[42] P. Lujan,[28] P. Lukens,[15] G. Lungu,[16] L. Lyons,[41] J. Lys,[28] R. Lysak,[1] D. MacQueen,[32] R. Madrak,[20] K. Maeshima,[15] P. Maksimovic,[24] L. Malferrari,[4] G. Manca,[29] R. Marginean,[38] M. Martin,[24] A. Martin,[59] V. Martin,[37] M. Martínez,[3] T. Maruyama,[54] H. Matsunaga,[54] M. Mattson,[57] P. Mazzanti,[4] K.S. McFarland,[47] D. McGivern,[30] P.M. McIntyre,[51] P. McNamara,[50] R. NcNulty,[29] S. Menzemer,[31] A. Menzione,[44] P. Merkel,[15] C. Mesropian,[48] A. Messina,[49] T. Miao,[15] N. Miladinovic,[5] L. Miller,[20] R. Miller,[34] J.S. Miller,[33] R. Miquel,[28] S. Miscetti,[17] G. Mitselmakher,[16] A. Miyamoto,[26] Y. Miyazaki,[40] N. Moggi,[4] B. Mohr,[7] R. Moore,[15] M. Morello,[44] A. Mukherjee,[15] M. Mulhearn,[31] T. Muller,[25] R. Mumford,[24] A. Munar,[43] P. Murat,[15] J. Nachtman,[15] S. Nahn,[59] I. Nakamura,[43] I. Nakano,[39] A. Napier,[55] R. Napora,[24] D. Naumov,[36] V. Necula,[16] F. Niell,[33] J. Nielsen,[28] C. Nelson,[15] T. Nelson,[15] C. Neu,[43] M.S. Neubauer,[8] C. Newman-Holmes,[15] A-S. Nicollerat,[18] T. Nigmanov,[45] L. Nodulman,[2] O. Norniella,[3] K. Oesterberg,[21] T. Ogawa,[56] S.H. Oh,[14] Y.D. Oh,[27] T. Ohsugi,[22] T. Okusawa,[40] R. Oldeman,[49] R. Orava,[21] W. Orejudos,[28] C. Pagliarone,[44] F. Palmonari,[44] R. Paoletti,[44] V. Papadimitriou,[15] S. Pashapour,[32] J. Patrick,[15] G. Pauletta,[53] M. Paulini,[11] T. Pauly,[41] C. Paus,[31] D. Pellett,[6] A. Penzo,[53] T.J. Phillips,[14] G. Piacentino,[44] J. Piedra,[10] K.T. Pitts,[23] C. Plager,[7] A. Pompoš,[46] L. Pondrom,[58] G. Pope,[45] O. Poukhov,[13] F. Prakoshyn,[13] T. Pratt,[29] A. Pronko,[16] J. Proudfoot,[2] F. Ptohos,[17] G. Punzi,[44] J. Rademacker,[41] A. Rakitine,[31] S. Rappoccio,[20] F. Ratnikov,[50] H. Ray,[33] A. Reichold,[41] B. Reisert,[15] V. Rekovic,[36] P. Renton,[41] M. Rescigno,[49] F. Rimondi,[4] K. Rinnert,[25] L. Ristori,[44] W.J. Robertson,[14] A. Robson,[41] T. Rodrigo,[10] S. Rolli,[55] L. Rosenson,[31] R. Roser,[15] R. Rossin,[42] C. Rott,[46] J. Russ,[11] A. Ruiz,[10] D. Ryan,[55] H. Saarikko,[21] A. Safonov,[6] R. St. Denis,[19] W.K. Sakumoto,[47] G. Salamanna,[49] D. Saltzberg,[7] C. Sanchez,[3] A. Sansoni,[17] L. Santi,[53] S. Sarkar,[49] K. Sato,[54] P. Savard,[32] A. Savoy-Navarro,[15] P. Schemitz,[25] P. Schlabach,[15] E.E. Schmidt,[15] M.P. Schmidt,[59] M. Schmitt,[37] L. Scodellaro,[42] A. Scribano,[44] F. Scuri,[44] A. Sedov,[46] S. Seidel,[36] Y. Seiya,[40] F. Semeria,[4] L. Sexton-Kennedy,[15] I. Sfiligoi,[17] M.D. Shapiro,[28] T. Shears,[29] P.F. Shepard,[45] M. Shimojima,[54] M. Shochet,[12] Y. Shon,[58] I. Shreyber,[35] A. Sidoti,[44] J. Siegrist,[28] M. Siket,[1] A. Sill,[52] P. Sinervo,[32] A. Sisakyan,[13] A. Skiba,[25] A.J. Slaughter,[15] K. Sliwa,[55] D. Smirnov,[36] J.R. Smith,[6] F.D. Snider,[15] R. Snihur,[32] S.V. Somalwar,[50]

J. Spalding,[15] M. Spezziga,[52] L. Spiegel,[15] F. Spinella,[44] M. Spiropulu,[9] P. Squillacioti,[44] H. Stadie,[25] A. Stefanini,[44] B. Stelzer,[32] O. Stelzer-Chilton,[32] J. Strologas,[36] D. Stuart,[9] A. Sukhanov,[16] K. Sumorok,[31] H. Sun,[55] T. Suzuki,[54] A. Taffard,[23] R. Tafirout,[32] S.F. Takach,[57] H. Takano,[54] R. Takashima,[22] Y. Takeuchi,[54] K. Takikawa,[54] M. Tanaka,[2] R. Tanaka,[39] N. Tanimoto,[39] S. Tapprogge,[21] M. Tecchio,[33] P.K. Teng,[1] K. Terashi,[48] R.J. Tesarek,[15] S. Tether,[31] J. Thom,[15] A.S. Thompson,[19] E. Thomson,[43] P. Tipton,[47] V. Tiwari,[11] S. Tkaczyk,[15] D. Toback,[51] K. Tollefson,[34] T. Tomura,[54] D. Tonelli,[44] M. Tönnesmann,[34] S. Torre,[44] D. Torretta,[15] S. Tourneur,[15] W. Trischuk,[32] J. Tseng,[41] R. Tsuchiya,[56] S. Tsuno,[39] D. Tsybychev,[16] N. Turini,[44] M. Turner,[29] F. Ukegawa,[54] T. Unverhau,[19] S. Uozumi,[54] D. Usynin,[43] L. Vacavant,[28] A. Vaiciulis,[47] A. Varganov,[33] E. Vataga,[44] S. Vejcik III,[15] G. Velev,[15] G. Veramendi,[23] T. Vickey,[23] R. Vidal,[15] I. Vila,[10] R. Vilar,[10] I. Volobouev,[28] M. von der Mey,[7] P. Wagner,[51] R.G. Wagner,[2] R.L. Wagner,[15] W. Wagner,[25] R. Wallny,[7] T. Walter,[25] T. Yamashita,[39] K. Yamamoto,[40] Z. Wan,[50] M.J. Wang,[1] S.M. Wang,[16] A. Warburton,[32] B. Ward,[19] S. Waschke,[19] D. Waters,[30] T. Watts,[50] M. Weber,[28] W.C. Wester III,[15] B. Whitehouse,[55] A.B. Wicklund,[2] E. Wicklund,[15] H.H. Williams,[43] P. Wilson,[15] B.L. Winer,[38] P. Wittich,[43] S. Wolbers,[15] M. Wolter,[55] M. Worcester,[7] S. Worm,[50] T. Wright,[33] X. Wu,[18] F. Würthwein,[8] A. Wyatt,[30] A. Yagil,[15] U.K. Yang,[12] W. Yao,[28] G.P. Yeh,[15] K. Yi,[24] J. Yoh,[15] P. Yoon,[47] K. Yorita,[56] T. Yoshida,[40] I. Yu,[27] S. Yu,[43] Z. Yu,[59] J.C. Yun,[15] L. Zanello,[49] A. Zanetti,[53] I. Zaw,[20] F. Zetti,[44] J. Zhou,[50] A. Zsenei,[18] and S. Zucchelli[4]

(The CDF II Collaboration)

[1]*Institute of Physics, Academia Sinica, Taipei, Taiwan 11529, Republic of China*
[2]*Argonne National Laboratory, Argonne, Illinois 60439*
[3]*Institut de Fisica d'Altes Energies, Universitat Autonoma de Barcelona, E-08193, Bellaterra (Barcelona), Spain*
[4]*Istituto Nazionale di Fisica Nucleare, University of Bologna, I-40127 Bologna, Italy*
[5]*Brandeis University, Waltham, Massachusetts 02254*
[6]*University of California at Davis, Davis, California 95616*
[7]*University of California at Los Angeles, Los Angeles, California 90024*
[8]*University of California at San Diego, La Jolla, California 92093*
[9]*University of California at Santa Barbara, Santa Barbara, California 93106*
[10]*Instituto de Fisica de Cantabria, CSIC-University of Cantabria, 39005 Santander, Spain*
[11]*Carnegie Mellon University, Pittsburgh, PA 15213*
[12]*Enrico Fermi Institute, University of Chicago, Chicago, Illinois 60637*
[13]*Joint Institute for Nuclear Research, RU-141980 Dubna, Russia*
[14]*Duke University, Durham, North Carolina 27708*
[15]*Fermi National Accelerator Laboratory, Batavia, Illinois 60510*
[16]*University of Florida, Gainesville, Florida 32611*
[17]*Laboratori Nazionali di Frascati, Istituto Nazionale di Fisica Nucleare, I-00044 Frascati, Italy*
[18]*University of Geneva, CH-1211 Geneva 4, Switzerland*
[19]*Glasgow University, Glasgow G12 8QQ, United Kingdom*

[20]Harvard University, Cambridge, Massachusetts 02138
[21]The Helsinki Group: Helsinki Institute of Physics; and Division of High Energy Physics, Department of Physical Sciences, University of Helsinki, FIN-00044, Helsinki, Finland
[22]Hiroshima University, Higashi-Hiroshima 724, Japan
[23]University of Illinois, Urbana, Illinois 61801
[24]The Johns Hopkins University, Baltimore, Maryland 21218
[25]Institut für Experimentelle Kernphysik, Universität Karlsruhe, 76128 Karlsruhe, Germany
[26]High Energy Accelerator Research Organization (KEK), Tsukuba, Ibaraki 305, Japan
[27]Center for High Energy Physics: Kyungpook National University, Taegu 702-701; Seoul National University, Seoul 151-742; and SungKyunKwan University, Suwon 440-746; Korea
[28]Ernest Orlando Lawrence Berkeley National Laboratory, Berkeley, California 94720
[29]University of Liverpool, Liverpool L69 7ZE, United Kingdom
[30]University College London, London WC1E 6BT, United Kingdom
[31]Massachusetts Institute of Technology, Cambridge, Massachusetts 02139
[32]Institute of Particle Physics: McGill University, Montréal, Canada H3A 2T8; and University of Toronto, Toronto, Canada M5S 1A7
[33]University of Michigan, Ann Arbor, Michigan 48109
[34]Michigan State University, East Lansing, Michigan 48824
[35]Institution for Theoretical and Experimental Physics, ITEP, Moscow 117259, Russia
[36]University of New Mexico, Albuquerque, New Mexico 87131
[37]Northwestern University, Evanston, Illinois 60208
[38]The Ohio State University, Columbus, Ohio 43210
[39]Okayama University, Okayama 700-8530, Japan
[40]Osaka City University, Osaka 588, Japan
[41]University of Oxford, Oxford OX1 3RH, United Kingdom
[42]University of Padova, Istituto Nazionale di Fisica Nucleare, Sezione di Padova-Trento, I-35131 Padova, Italy
[43]University of Pennsylvania, Philadelphia, Pennsylvania 19104
[44]Istituto Nazionale di Fisica Nucleare, University and Scuola Normale Superiore of Pisa, I-56100 Pisa, Italy
[45]University of Pittsburgh, Pittsburgh, Pennsylvania 15260
[46]Purdue University, West Lafayette, Indiana 47907
[47]University of Rochester, Rochester, New York 14627
[48]The Rockefeller University, New York, New York 10021
[49]Istituto Nazionale di Fisica Nucleare, Sezione di Roma 1, University di Roma "La Sapienza," I-00185 Roma, Italy
[50]Rutgers University, Piscataway, New Jersey 08855
[51]Texas A&M University, College Station, Texas 77843
[52]Texas Tech University, Lubbock, Texas 79409
[53]Istituto Nazionale di Fisica Nucleare, University of Trieste/ Udine, Italy
[54]University of Tsukuba, Tsukuba, Ibaraki 305, Japan
[55]Tufts University, Medford, Massachusetts 02155
[56]Waseda University, Tokyo 169, Japan
[57]Wayne State University, Detroit, Michigan 48201
[58]University of Wisconsin, Madison, Wisconsin 53706

[59] *Yale University, New Haven, Connecticut 06520*
(Dated: September 13, 2004)

Abstract

We report a measurement of the $t\bar{t}$ production cross section using the CDF II detector at the Fermilab Tevatron. The data consist of events with an energetic electron or muon, missing transverse energy, and three or more hadronic jets, at least one of which is identified as a b-quark jet by reconstructing a secondary vertex. The background fraction is determined from a fit of the transverse energy of the leading jet. Using 162 ± 10 pb^{-1} of data, the total cross section is found to be 6.0 ± 1.6(stat.)±1.2(syst.) pb, which is consistent with the Standard Model prediction.

PACS numbers: 14.65.Ha, 13.85.Ni, 13.85.Qk

The top quark is the most massive of nature's building blocks yet discovered. Because new physics associated with electroweak symmetry breaking will likely couple to an elementary particle in proportion to its mass, it is important to measure the top quark couplings as accurately as possible. In the strong interaction sector, the couplings are reflected in the $t\bar{t}$ production cross section in hadron collisions. Previous measurements were made in $p\bar{p}$ collisions at a center-of-mass energy of 1.8 TeV [1]. We recently reported a result [2], using data taken at 1.96 TeV with the CDF II detector at the Tevatron collider, using the double leptonic decay mode of the top quark. Here we report a measurement of the $t\bar{t}$ production cross section using a different decay mode and a new method.

In order to measure the cross section, one first has to obtain a sample rich in top quarks and then determine the amount of background in the sample. We select events consistent with the decay chain $t\bar{t} \rightarrow WbW\bar{b} \rightarrow l\nu bq\bar{q}'\bar{b}$, where the charged lepton l is either an electron or muon. We start with events containing an energetic electron or muon, significant transverse momentum imbalance indicative of a non-interacting neutrino, and at least three hadronic jets. To enrich the sample in top quarks, we require that at least one jet contain a secondary vertex consistent with the decay of a B hadron.

Measurements in the past have relied on the ability of theoretical calculations to determine, for the background, the fraction of events that contain b-quark jets. In this paper, we instead measure the background fraction directly in the signal data sample. The transverse energy of the highest E_T jet [3] or the second highest E_T jet is a good discriminator between signal and background. Typically in a $t\bar{t}$ event, these jets are the primary decay products (b-jets) of the very heavy top quarks and thus have a hard E_T spectrum. For most of the background sources, however, they are produced as QCD radiation, resulting in a much softer bremsstrahlung-like E_T distribution. We use the leading jet E_T spectrum for the primary measurement of the signal fraction. The second leading jet distribution is used to check the result.

In order to obtain the background spectrum, we need data that are kinematically similar to our final sample, but which do not have significant $t\bar{t}$ contamination. We show that the leading jet E_T spectra for the background processes are similar whether or not the events contain b-quark jets. Then the non-heavy flavor spectrum becomes the background template for measuring the $t\bar{t}$ fraction in the signal sample.

We use the HERWIG [4] and PYTHIA [5] Monte Carlo calculations followed by a simulation of the CDF II detector to obtain the $t\bar{t}$ signal behavior. The soft E_T spectrum of the parton showers in these Monte Carlo models is not relevant for the signal shape. To test that our method is plausible, we study the background shape using the ALPGEN+HERWIG Monte Carlo [6]. ALPGEN provides a harder and more realistic jet E_T spectrum. For the study of b-jet identification, the PYTHIA calculation is used.

The CDF II detector [7] is an azimuthally and forward-backward symmetric apparatus designed to study $p\bar{p}$ collisions at the Fermilab Tevatron. It consists of a magnetic spectrometer surrounded by calorimeters and muon chambers. The charged particle tracking system is immersed in a 1.4 T magnetic field parallel to the p and $\bar{p}$ beams. A 700,000-channel silicon microstrip detector (SVX+ISL) provides tracking over the radial range from 1.5 to 28 cm. A 3.1 m long open-cell drift chamber, the Central Outer Tracker (COT), covers the radial range from 40 to 137 cm. The COT provides up to 96 measurements of the track position with alternating axial and 2° stereo superlayers of 12 wires each. The fiducial region of the silicon detector extends to $|\eta| \sim 2$, while the COT provides coverage for $|\eta| \leq 1$.

Segmented electromagnetic and hadronic calorimeters surround the tracking system and

measure the energy of interacting particles. The electromagnetic and hadronic calorimeters are lead-scintillator and iron-scintillator sampling devices, respectively, covering the pseudorapidity range $|\eta| < 3.6$. The electromagnetic calorimeters are instrumented with proportional and scintillating strip detectors that measure the transverse profile of electromagnetic shower candidates at a depth corresponding to the shower maximum. Drift chambers located outside the central hadron calorimeters and behind a 60 cm iron shield detect muons with $|\eta| < 0.6$. Additional drift chambers and scintillation counters detect muons in the region $0.6 < |\eta| < 1.0$. Gas Cherenkov counters measure the average number of inelastic $p\bar{p}$ collisions and thereby determine the luminosity with the coverage $3.7 < |\eta| < 4.7$.

The results reported here are based on data taken in Fermilab Collider Run II between March, 2002 and September, 2003. The integrated luminosity is 162 pb^{-1} for events selected with an electron or central muon. For muon events with $|\eta|$ between 0.6 and 1.0, the integrated luminosity is 150 pb^{-1}.

CDF employs a three level trigger system, the first two consisting of special purpose hardware and the third a farm of computers. For the electron top sample, the level-1 trigger requires a track of $P_T > 8$ GeV/c matched to an electromagnetic calorimeter cell containing $E_T > 8$ GeV with a small amount of energy in the hadronic cell behind it. Calorimeter energy clustering is done at level-2, and the ≥ 8 GeV/c track must be matched to an electromagnetic cluster with E_T above 16 GeV. At level-3, a reconstructed electron candidate with $E_T > 18$ GeV is required. The $P_T > 18$ GeV/c level-3 muon triggers come directly from two level-1 triggers: a track with $P_T > 4$ GeV/c is matched to a stub in the central muon chambers; or a track with $P_T > 8$ GeV/c is matched to a stub in the $0.6 < |\eta| < 1.0$ muon chambers.

After full event reconstruction, we require lepton candidates to pass identification criteria and to be isolated from other energy deposits in the calorimeter. The event selection criteria are the same as those in Ref. [8], where they are described in detail. Electron candidates must have a well-measured track pointing at a cluster of energy in the calorimeter with $E_T > 20$ GeV. The lateral and transverse shower size in the calorimeters as well as the transverse profile in the shower-maximum detectors must be consistent with an electromagnetic cascade. Muon candidates with $P_T > 20$ GeV/c must pass through calorimeter cells whose energy deposition is consistent with the ionization of a muon, and the reconstructed position of the track segment in the muon chambers is required to be consistent with multiple Coulomb scattering of the extrapolated track from the COT. In addition, all candidate events must have $\not\!\!E_T > 20$ GeV. The $\not\!\!E_T$ is corrected for both muon momentum and the position of the $p\bar{p}$ collision point. Jets are found using a fixed-cone algorithm with a cone radius of 0.4 in η-ϕ space. To obtain the correct jet energy, this analysis applies four corrections after jet clustering. We correct for detector response variations in η, detector stability, energy response nonlinearity, and a correction for multiple interactions in an event. For this analysis, jets are counted if they have $E_T > 15$ GeV and $|\eta| < 2.0$ after all the corrections are applied. We select events with three or more jets to retain high acceptance for $t\bar{t}$ events, allowing one jet to fail our E_T or η requirement.

In this sample, the major background to $t\bar{t}$ is the electroweak production of a W boson with hadron jets produced by QCD. These W + jets events usually contain only light quark and gluon jets, whereas signal events always contain two b-quark jets. Thus identification of b-jets (b-tag) provides a significant increase in the signal-to-background ratio.

We identify b-quark jets through the metastable B hadrons in the jet fragmentation.

Their ~ 1 ps lifetime translates into a secondary vertex a few millimeters from the primary interaction. We use the excellent position resolution of the SVX+ISL to find these secondary vertices. The algorithm [9] proceeds as follows: (1) select at least two good tracks in a jet with both COT and SVX+ISL information, (2) search for a high quality secondary vertex using the selected tracks, (3) measure the distance in the transverse plane (L_T) between the primary and the secondary vertices, and (4) accept the secondary vertex if $L_T/\sigma(L_T) > 3$, where $\sigma(L_T)$ is the L_T resolution.

Based on simulation of the b-tagging algorithm, we determined that requiring at least one of the jets in an event to be tagged as a b-jet is expected to retain 53% of the top quark events while removing more than 95% of the background events [9]. The measured cross section depends on the value of the b-tagging efficiency used to extract it. The difference between the efficiency in the simulation and that in data has been measured with a b-enriched sample of dijet events in which an electron is found in one jet. We find that the simulation has a b-tag efficiency higher than the data by 21%, a factor that is independent of jet E_T [9]. This difference is corrected for and the uncertainty is discussed below.

There are several background sources in the b-tagged $l + \not\!\!E_T + \geq 3$ jets sample. These are the production of a W boson accompanied by the QCD production of heavy flavor quarks (W+HF: $39.8 \pm 7.0\%$ of the total number of the background events in $W+ \geq 3$ jets), mis-identification in b-jet tagging mainly due to track and vertex resolution (mistag: $29.6 \pm 4.9\%$), a fake W boson associated with a real or fake lepton (non-W: $21.0 \pm 4.5\%$), diboson production ($WW/WZ/ZZ$) and electroweak $t\bar{b}$ production (diboson + single top: $9.6 \pm 1.7\%$) [9].

In this paper, we use the shape of the leading jet E_T spectrum to determine the signal and background fractions. We have determined that the leading jet E_T is the best discriminant between the signal and background among single jet E_T variables after considering both statistical and systematic effects. For the background, we extract from data the shape for all of the sources except for the small diboson and single top components. We assume that the W+HF and mistag shapes are the same, so that we can extract that distribution from the background-rich sample of events in which no jet is b-tagged, but at least one jet is taggable, i.e., has at least two good tracks that pass through the SVX+ISL detector. This assumption is supported by a Leading-Order (LO), and a Next-to-Leading-Order (NLO) simulation [10]. Since the difference between LO and NLO is smallest for the leading jet E_T variable, we use it for the analysis. The method is tested with data events containing a W boson and either 1 or 2 jets. Figure 1 shows the shape comparison of the highest jet E_T between $W+$ three light flavor jets (W+LF) and the various heavy flavor contributions as predicted by ALPGEN+HERWIG Monte Carlo calculation followed by a simulation of the CDF II detector. In W+HF cases, at least one jet is required to be b-tagged, while for W+LF, we perform the same procedure as mentioned below to predict the W+HF shapes from data. To determine this spectrum from data, we use events in which at least one jet is taggable, but none is b-tagged. This minimizes the $t\bar{t}$ contamination in the background shape. Before using this shape to predict the b-tagged sample, we have to take into account the variation of the b-tag efficiency with jet E_T. The shape of the b-tag efficiency, which is approximately flat except at low E_T, is taken from simulation (Fig. 2).

The leading jet E_T spectrum shape of mistagged events is not *a priori* the same as the W+HF shape, where the b-jets are tagged, since the shapes may depend on the b-tagging algorithm. However, the current algorithm provides similar leading jet E_T spectra. Figure 3 shows the b-tag rate and the mistag rate as a function of the jet E_T obtained from the CDF

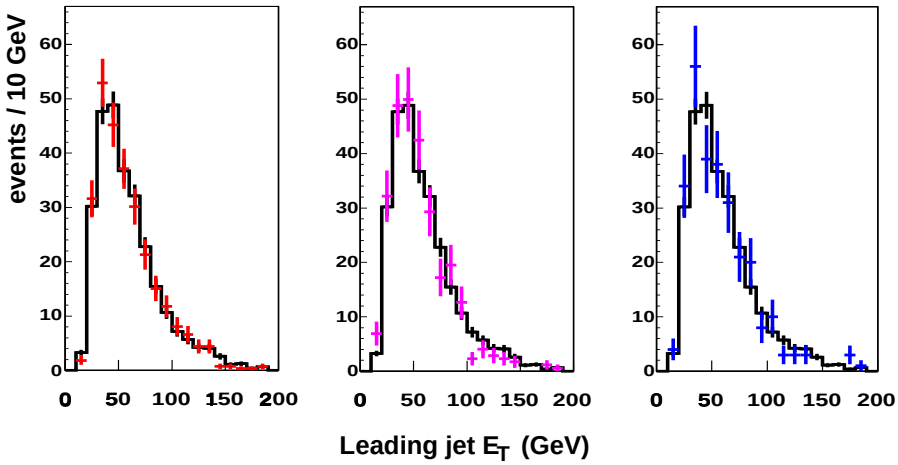

FIG. 1: The leading jet E_T spectrum for W plus three light flavor jets (solid histogram in all plots) compared to $Wb\bar{b}$ plus one light quark (left), Wc plus two light quarks (center), and $Wc\bar{c}$ plus one light quark (right). These are ALPGEN+HERWIG Monte Carlo calculations followed by a simulation of the CDF II detector. (normalized by area)

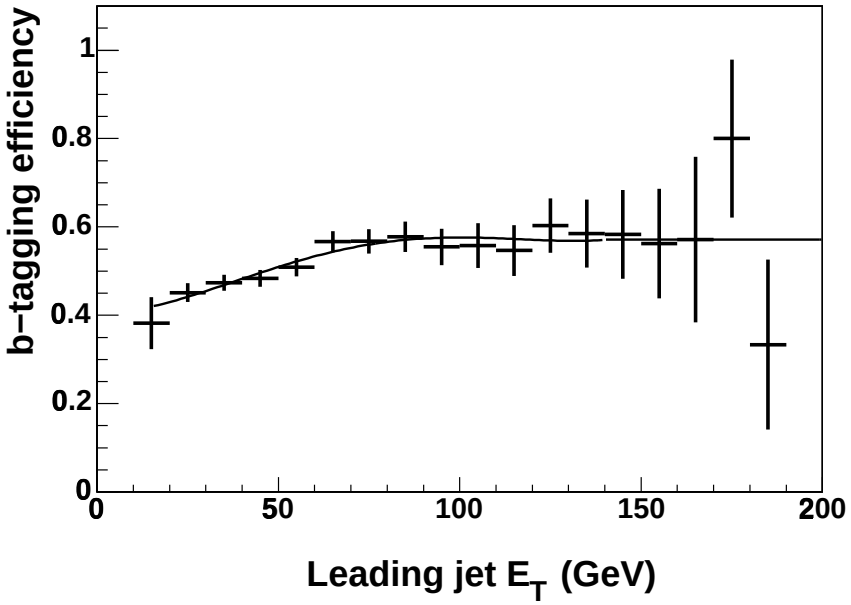

FIG. 2: The efficiency of b-jet identification as a function of the leading jet E_T derived from ALPGEN $Wb\bar{b}$ Monte Carlo in the $W+ \geq 3$-jet sample. The curve is a fourth-degree polynomial fit below 140 GeV.

II jet sample. We apply the mistag rate obtained from data to the W+LF simulation, and compare it to W+HF (Fig. 4). These shapes agree well and therefore the assumption is still valid.

The other large background comes from events that do not contain a W boson. The lepton candidate is either misidentified or due to semi-leptonic decay in a b- or c-jet. Such

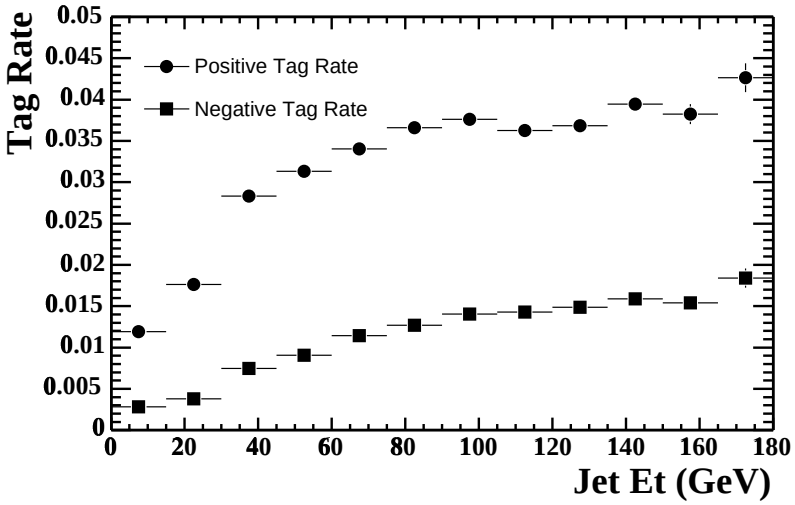

FIG. 3: The b-tag (positive tag in figure) rate and the mistag (negative tag) rate as a function of the jet E_T obtained from the jet data sample [9]. We use a generic jet sample that does not include any significant number of W bosons. The b-jet identification algorithm gives similar shapes for the b-tag and mistag rates.

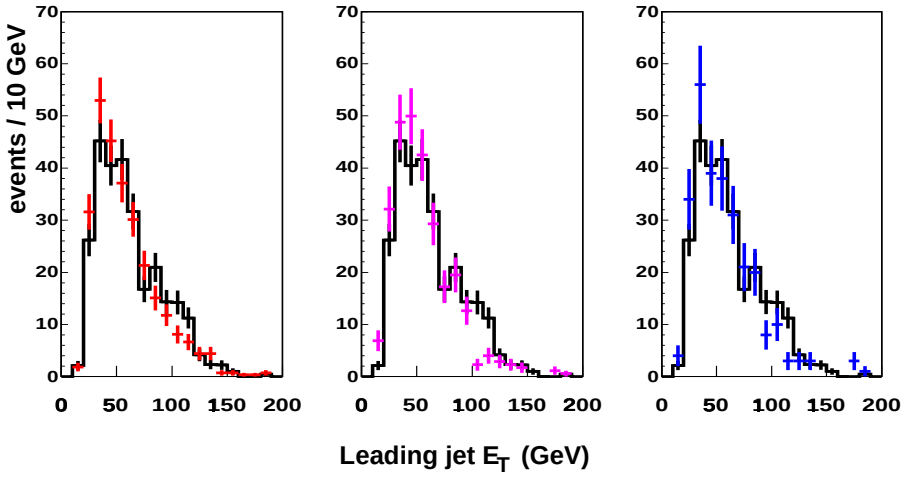

FIG. 4: The leading jet E_T spectrum for mistagged W plus three light flavor jets (solid histogram in all plots) compared to $Wb\bar{b}$ plus one light quark (left), Wc plus two light quarks (center), and $Wc\bar{c}$ plus one light quark (right). Note that the mistag prediction is realistic since it is obtained from jet data

leptons are typically not isolated in the calorimeter. Consequently the shape of the leading jet E_T spectrum for non-W events is determined from events that still have large missing transverse energy ($\not\!\!E_T > 20$ GeV), but whose lepton is not isolated. Isolation is defined as the ratio between calorimeter energy in a cone of radius 0.4 in the η-ϕ plane around the lepton, but excluding the lepton, divided by the lepton energy. We assume that the leading jet E_T shape of this sample is the same as for the non-W background events in the signal

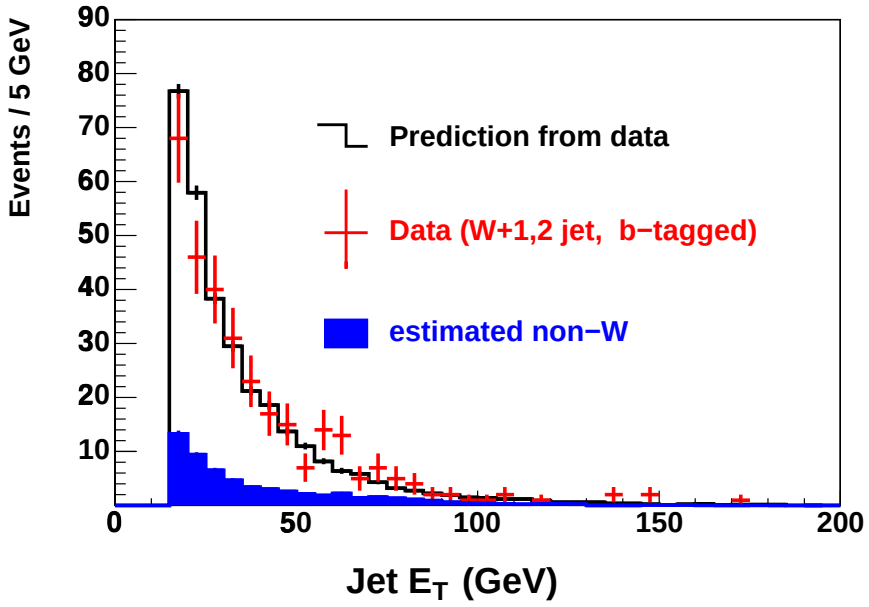

FIG. 5: The leading jet E_T distribution for the 309 jets in the W+1 and 2 jet data sample. The open histogram is the total background prediction, with the dark shaded region the non-W component. The data points are the b-tagged events with statistical error bars.

region since lepton isolation is not correlated with the E_T of other jets in an event. The non-W background distribution is added to the other backgrounds with a relative normalization taken from absolute estimates of the various background sources. However, since the non-W jet E_T spectrum is very similar to those in the W+HF and mistag backgrounds, the final result is insensitive to the non-W fraction. A systematic uncertainty is taken based on a large variation in this background fraction.

The spectra from diboson and single top production are estimated from ALPGEN+ HERWIG Monte Carlo calculations. The leading jet E_T spectrum from single top production is added to the total background shape using the theoretical cross section, which is 6% of the total background, while the diboson spectra are neglected because these spectra are similar to the other dominant background sources, and their contribution is expected to be small, $\sim$ 3.0% [11].

The performance of the background modeling is tested using events containing a high P_T lepton, large $\not\!\!E_T$, and either 1 or 2 jets (recall the signal sample uses 3 or more jets). This sample contains all of the signal region background sources, but the $t\bar{t}$ contribution is small, only $\sim$ 4%. A similar procedure is applied here as in the $W+ \geq$ 3-jet sample. The dominant background shape is taken from events without a b-tag, but with at least one taggable jet, and then a non-W contribution is added with a fraction ($\sim$ 15.2%) determined from absolute background estimates [9]. A correction is made for the E_T dependence of the b-tagging efficiency. The resulting spectrum should agree well with that of the b-tagged events if our method is valid. Figure 5 shows the results using 309 jets in the W+1 and 2 jet samples. The agreement is good, with a Kolmogorov-Smirnov (KS) test probability of 18%. This value is not the KS probability itself but the p-value based on pseudo-experiments using the maximum difference of the accumulating distributions.

The E_T spectra of the four main backgrounds in the signal sample, $W+ \geq$3 jets, are

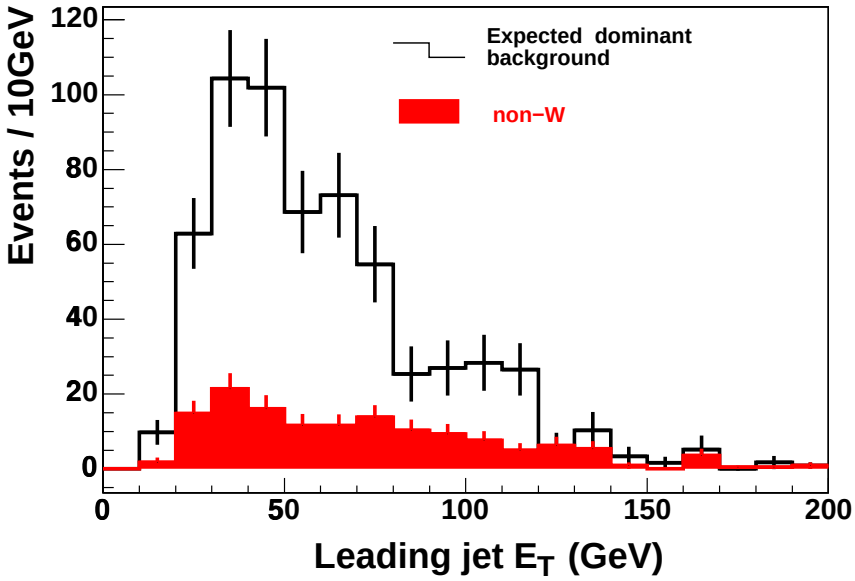

FIG. 6: The calculated dominant background shape (W+HF, mistag, non-W) in $W+\geq 3$ jets sample. The shaded part is the non-W portion. Error bars are statistical only.

shown in Fig. 6. The dominant contribution is taken from the non-b-tagged events (W+HF, mistag). These spectra have been corrected for the shape of the b-tag efficiency, which has been determined from simulation, and is shown in Fig. 2 as a function of the jet E_T . The small $t\bar{t}$ contamination, $\sim 6\%$, in the non-b-tagged sample is subtracted iteratively, as described below, so that the amount of this contamination is consistent with the final $t\bar{t}$ cross section. The non-W component is 21% of the total and is shown as the shaded portion. The small contribution from single-top production is then added, and the diboson components ($WW/WZ/ZZ$) are neglected as noted above.

As indicated above, the shape change due to the application of the b-tagging algorithm is applied to the background spectra. The efficiency of the algorithm is defined as the number of events that have at least one b-tagged jet divided by the number having at least one taggable jet. This function, which drops at very low E_T, is fit to a fourth-degree polynomial below 140 GeV and a flat line above 140 GeV. Possible variations in this shape are considered as a systematic uncertainty on the cross section measurement. Note that only the shape, not the absolute efficiency, is used here.

The final background shape is shown in Fig. 7. We fit this shape for use in the final unbinned log-likelihood fit using a Landau distribution plus a Gaussian function. The fitted parameters are summarized in Table I, and the fit result is shown in Fig. 7. The $\chi^2/d.o.f.$ for the agreement between the fit function and the data points is 11.4/10.

We use a HERWIG Monte Carlo calculation followed by a full detector simulation to obtain the $t\bar{t}$ signal shape. Figure 8 shows the predicted leading jet E_T distribution for $t\bar{t}$ events. It is significantly harder than the background spectrum, making it possible to separate the two contributions using a fit to the data. The spectrum in Fig. 8 is fit to a Landau distribution plus two Gaussians ($\chi^2/d.o.f. = 19.9/28$). The fitted parameters are shown in Table II.

To fit the data to a sum of the signal and background templates, we use an unbinned

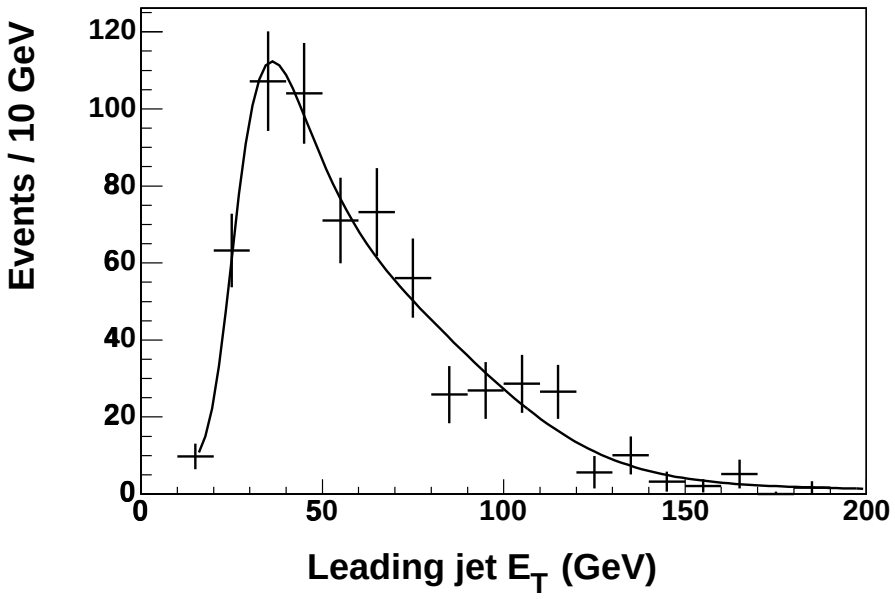

FIG. 7: The calculated leading jet E_T distribution for the background in the $W+ \geq 3$-jet sample. The fitted curve shows the Landau plus Gaussian function that is employed in the final unbinned likelihood fit.

TABLE I: Presented in this table are the fit parameters used to describe the background probability density function shown in Fig. 7. (L) and (G) refer to the Landau function and Gaussian parameters, respectively. The variable MPV represents the most probable value of Landau function. The means and sigmas are expressed in GeV.

parameters	values
height(G)	30.80±10.27
mean(G)	66.71±7.4
sigma(G)	32.77±5.6
height(L)	512.8±79.2
MPV(L)	37.0±3.6
sigma(L)	7.67±1.5

likelihood fit with the following form.

$$\begin{aligned}\mathcal{L} &= \prod_{i=1}^{N} P(E_{Ti}; R) \\ &= \prod_{i=1}^{N} [R\, P_{\text{signal}}(E_{Ti}) + (1-R)\, P_{\text{background}}(E_{Ti})]\end{aligned}$$

where the signal fraction R=$\frac{N_{\text{signal}}}{N_{\text{signal}}+N_{\text{background}}}$ is the one free parameter in the fit, $P_{\text{signal}}(E_{Ti})$ is the signal probability density as a function of E_T, and $P_{\text{background}}(E_{Ti})$ is that of the background. We tested the ability of this fit procedure to report correct values of the signal

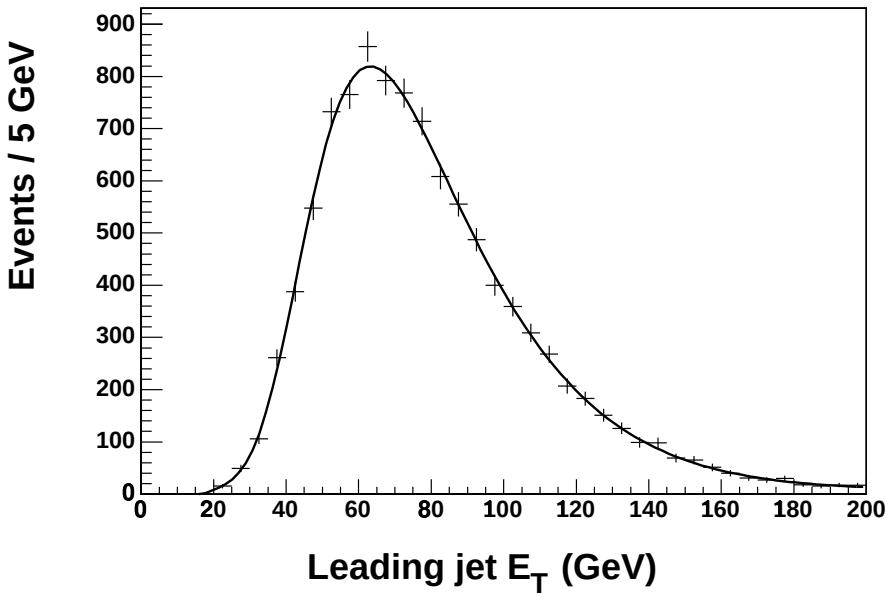

FIG. 8: The simulated leading jet E_T spectrum for $t\bar{t}$ events for the top mass 175 GeV/c^2. The smooth curve is a fit to a Landau distribution plus two Gaussians.

TABLE II: Fit parameters for the $t\bar{t}$ leading jet E_T distribution in Fig. 8 using two Gaussians and a Landau distribution. (L) and (G) refer to the Landau and Gaussian parameters, respectively. The variable MPV represents the most probable value of Landau function. The means and sigmas are expressed in GeV.

parameters	values
height(G1)	200.8±26.0
mean(G1)	60.0±5.0
sigma(G1)	35.6±1.1
height(G2)	-109.9±8.3
mean(G2)	-76.1±6.5
sigma(G2)	192.9±14.3
height(L)	3913.5±192.8
MPV(L)	65.8±1.1
sigma(L)	13.9±0.6

fraction and its uncertainty using a large number of Monte Carlo pseudo-experiments. Each pseudo-experiment used the number of signal and background events in our data sample and used a range of signal fractions (R) centered around the value found from our fit to the data.

As mentioned above, there is a small $t\bar{t}$ contamination in the untagged data sample that is used to create the background template. The amount of $t\bar{t}$ that is subtracted when making the template is determined by an iterative process. Initially the fit is done without removing a $t\bar{t}$ component from the background template. The number of top events reported by the fit is used along with the b-tagging efficiency to calculate the number of top events in the

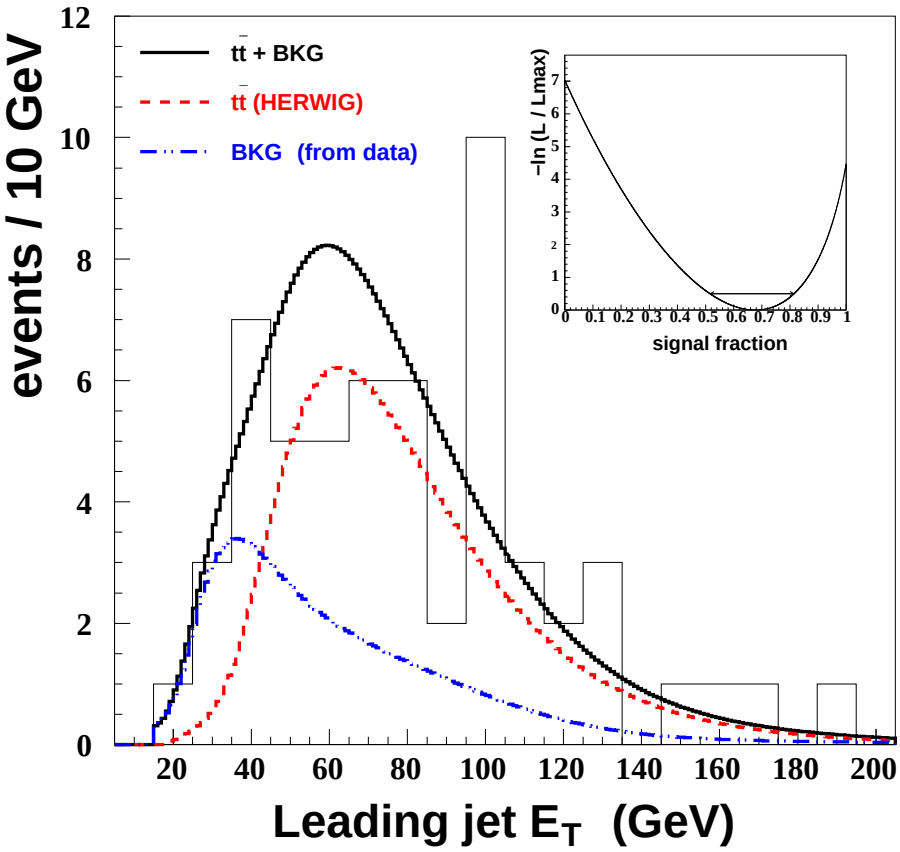

FIG. 9: The fifty-seven candidate events (histogram) with the best fit curve (solid). The best fit composition, $t\bar{t}$ (dashed) and background (dot-dashed), is also shown. The insert shows $-\ln(\mathcal{L}/\mathcal{L}_{\rm max})$ as a function of the signal fraction.

untagged sample. A $t\bar{t}$ subtraction in the background template is then made, and the data are refit. This $t\bar{t}$ contamination is determined to be small, $\sim 6\%$, thus only one iteration is necessary. The final background template after the iteration is shown in Fig. 7.

The result of the fit of the $W+ \geq 3$-jet data sample is shown in Fig. 9. The histogram contains the 57 data events in which at least one jet has been tagged as a b-jet. The solid curve is the best fit, with the individual components shown as dashed ($t\bar{t}$) and dot-dashed (background) curves. The insert contains $-\ln(\mathcal{L}/\mathcal{L}_{\rm max})$ as a function of signal fraction. The signal fraction obtained is $R = 0.68^{+0.14}_{-0.16}$.

Although we selected the leading jet E_T as the fit variable *a priori*, we have studied other variables to check the robustness of the result. For the second leading jet E_T and the sum of the first and second leading jet E_T's, we find signal fractions of $R = 0.75^{+0.11}_{-0.13}$ (Fig. 10) and $R = 0.65^{+0.14}_{-0.16}$ (Fig. 11), respectively. The agreement is good.

The $t\bar{t}$ cross section is obtained from the formula,

$$\sigma(t\bar{t}) = \frac{N_{\rm obs}\, R_{\rm fit}}{A_{t\bar{t}}\, \epsilon_{t\bar{t}} \int \mathcal{L} dt} \qquad (1)$$

where $N_{\rm obs}$ is the number of candidate $W+ \geq 3$-jet events with at least one b-tagged jet (57 events), $R_{\rm fit}$ is the signal fraction determined from the likelihood fit, and $A_{t\bar{t}}$ is the geometric

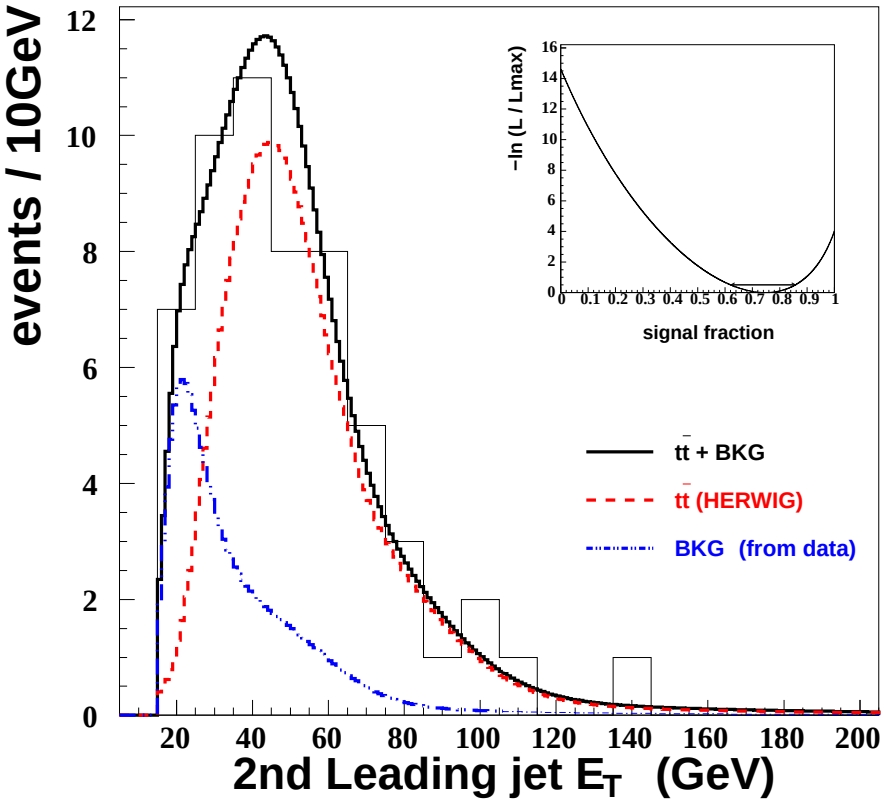

FIG. 10: The fit result using the second leading jet. The fifty-seven candidate events (histogram) with the best fit curve (solid). The best fit composition, $t\bar{t}$ (dashed) and background (dot-dashed), is also shown. The insert shows $-\ln(\mathcal{L}/\mathcal{L}_{\max})$ as a function of the signal fraction.

acceptance for $t\bar{t}$ events in the CDF II detector [8]. Note that this acceptance includes the branching ratios. The parameter $\epsilon_{t\bar{t}}$ is the detector efficiency for $t\bar{t}$ events [9], which includes the trigger, event vertex position, event b-tagging, and the lepton identification efficiencies. It also includes the effects due to photon conversion, cosmic ray, dilepton, and Z^0 boson removal. The quantity $\int \mathcal{L}dt$ is the integrated luminosity. The term $A_{t\bar{t}}\epsilon_{t\bar{t}}$ was determined from a PYTHIA Monte Carlo [5] calculation and detector simulation with a number of individual efficiency components determined from the data. The result for $A\epsilon$ is 4.02 ± 0.03(stat.)±0.43(syst.)%. The acceptance come from the electrons channel is $\sim$ 57%. All calculations have been done using a top quark mass of 175 GeV/c^2 [12]. Multiplying $A\epsilon$ by the integrated luminosity gives the denominator for the equation (1), 6.42 ± 0.8 pb^{-1}.

There are a number of sources of systematic uncertainty as summarized in Table III. Template shape uncertainties affect the signal fraction determination, while other effects mostly impact the acceptance. Systematic uncertainties in the signal fraction are determined by a series of pseudo-experiments in which the templates are changed and the data are then refit. If the systematic uncertainty affects both the template shapes and the acceptance the uncertainty is taken to be 100% correlated.

The largest uncertainty originates from the effect of the jet energy scale on the $t\bar{t}$ simulation. This comes from a number of sources including modeling the relative calorimeter response as a function of η, the absolute hadron energy scale, the underlying event contri-

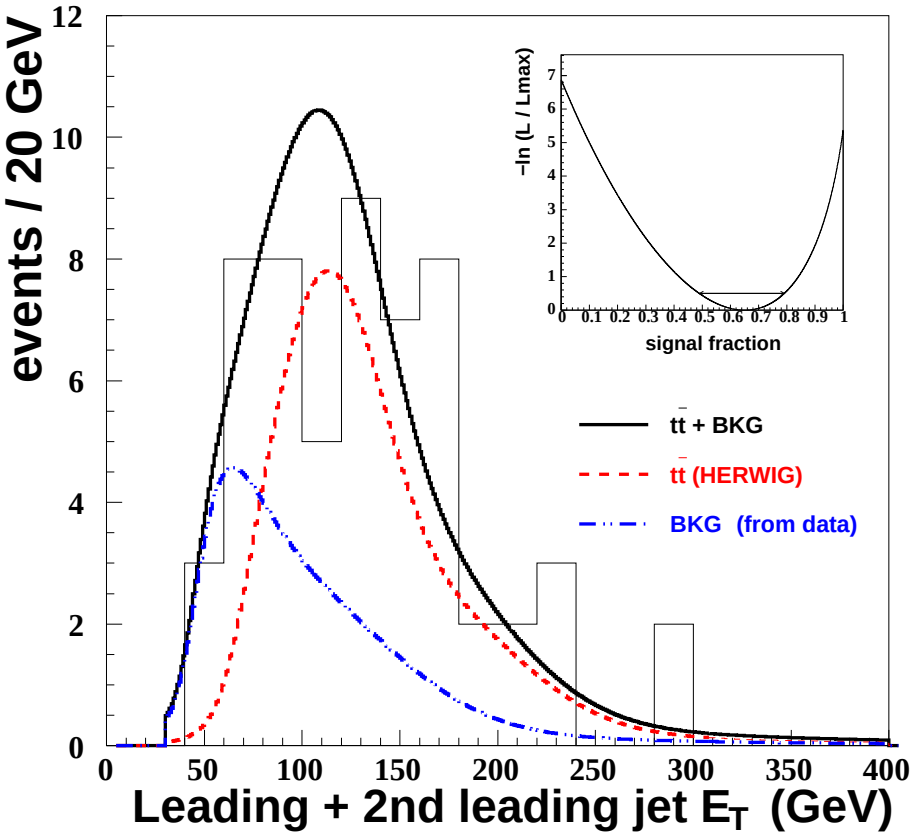

FIG. 11: The fit result using the sum of the leading and the second leadind jets. The fifty-seven candidate events (histogram) with the best fit curve (solid). The best fit composition, $t\bar{t}$ (dashed) and background (dot-dashed), is also shown. The insert shows $-\ln(\mathcal{L}/\mathcal{L}_{\max})$ as a function of the signal fraction.

bution, and jet fragmentation [8]. The largest contributions are due to the η correction of the jet energy and the energy scale uncertainty. The mean energy of the leading jet from top quark decay is varied by $\pm 6.1\%$, or about 5 GeV, and this effect contributes 15.3% to the final top cross section uncertainty. The jet energy scale uncertainty does not contribute to the background template shape systematic uncertainty largely because it is determined from the data.

There are uncertainties in both the absolute value and E_T dependence of the b-tag efficiencies, which are determined from b-jet rich and generic-jet control samples [9]. The uncertainty of the absolute b-tagging efficiency is dominated by several sources: statistics of the control data and Monte Carlo sample, composition uncertainties of the control sample and the branching ratio of the b semi-leptonic decay. The ratio of the b-tag efficiency between the Monte Carlo and b-jet rich control data sample is formed, and we vary the value within the uncertainties to determine the change in cross section. The E_T dependence of the b-tag efficiency uncertainty is determined using the slope difference of two ratios. We form as a function of E_T the b-tag efficiency ratio from the generic-jet data and the Monte Carlo simulation (slope and uncertainty), and also from the b-jet rich data sample and Monte Carlo simulation. A weighted average of the two slopes is used to determine the overall

slope uncertainty, which is then applied to the Monte Carlo simulation to determine the top quark cross section uncertainty.

The uncertainty in the background shape due to the statistics of the background sample is estimated with a series of pseudo-experiments in which the contents of each bin in Fig. 7 is varied independently according to Poisson statistics, with the resulting distribution refit to get a new background spectrum. The luminosity uncertainty comes predominantly from the uncertainty in the total inelastic cross section. Uncertainties in the lepton identification efficiency, which affect the acceptance, are determined from events using the unbiased tracks of $Z \to ll$ decays in events with multiple jets [8, 9]. There are several other efficiency uncertainties due to the trigger efficiency, the photon conversion veto efficiency, the cosmic ray veto efficiency, and track finding efficiency. These systematic uncertainties are summarized in table III.

The parton distribution functions for (anti-)protons affect not only the shape of the $t\bar{t}$ signal, but also the acceptances. These uncertainties are estimated by varying α_s and the parton distribution functions within the universal fit uncertainty [8]. There are also uncertainties from the amount of gluon radiation in the Monte Carlo generators. The amount of initial state radiation is studied using high mass Drell-Yan dilepton data. The non-W contribution to the background shape has an uncertainty both in its relative amount (to the overall background) and its shape. The former is estimated by a $\pm 100\%$ variation in the amount of background measured from the non-isolated lepton sample. The shape uncertainty is measured by changing the nominal mixture of events containing non-isolated electron and muon candidates ($\sim 3.7:1$ electrons to muons) in the data control sample to either 100% electrons or 100% muons. The shapes are used in the fit and the change in top quark cross section is reported as the systematic uncertainty.

There are shape uncertainties for those spectra obtained from simulation: $t\bar{t}$ and electroweak $t\bar{b}$ production. The uncertainty due to the $t\bar{t}$ shape comes from the difference between PYTHIA [5] and HERWIG [4] simulations. The theoretical electroweak single top quark $t\bar{b}$ production cross section uncertainty is small, which are known to about 3% [13]. We conservatively apply an uncertainty of 30% to the single top cross section. A background shape uncertainty also results from the uncertainty in the size of the $t\bar{t}$ contamination in the taggable but untagged sample and is negligible as we discussed above. The shape difference between the mistag and W+HF, shown in Fig. 4, is small compared to other systematics.

In conclusion, we have measured the $t\bar{t}$ production cross section in the lepton plus $\not\!\!E_T$ plus jets channel. $W+ \geq 3$ jets events were selected with at least one jet identified as a b-jet through secondary vertex reconstruction. Signal and background were separated using the shape of the leading jet E_T distribution. The measured total $t\bar{t}$ cross section is $6.0^{+1.5}_{-1.6}(\text{stat.})^{+1.2}_{-1.3}(\text{syst.})$ pb where we have assumed a top quark mass of 175 GeV/c^2 [12]. This is consistent with the Standard Model prediction [14] and with the recent result from CDF in the dilepton channel ($7.0^{+2.4+1.6}_{-2.1-1.1} \pm 0.4$ pb) [2]. The measured cross section depends on the top mass since a heavier top produces more energetic jets. This affects both the signal-background shape discrimination and the acceptance. A change in the top mass of $\pm$ 5 GeV/c^2 [12] alters the cross section by 6–8% as shown in Table IV.

This result also demonstrates that kinematic determination of the signal fraction using the leading jet E_T provides good signal to background discrimination. This technique can be used as an effective constraint in future $t\bar{t}$ measurements, such as the top quark mass. This method accounts properly for statistical fluctuation of the background because the signal to noise ratio is determined from the sample itself.

TABLE III: Systematic uncertainties for the $t\bar{t}$ cross section are combined assuming they are uncorrelated.

source	shape	acceptance	total
jet energy scale	$\pm 10.8\%$	$\pm 4.5\%$	$\pm 15.3\%$
absolute b-tag effic.	—	$\pm 7.4\%$	$\pm 7.4\%$
background statistics	$^{+2.6\%}_{-6.9\%}$	—	$^{+2.6\%}_{-6.9\%}$
luminosity	—	$\pm 5.9\%$	$\pm 5.9\%$
lepton ID	—	$\pm 5.0\%$	$\pm 5.0\%$
b-tag effic. (E_T dependence)	$\pm 1.9\%$	$\pm 2.5\%$	$\pm 4.4\%$
parton distribution function	$\pm 3.4\%$	$\pm 0.8\%$	$\pm 4.2\%$
gluon radiation	$\pm 0.9\%$	$\pm 2.6\%$	$\pm 3.5\%$
non-W (shape)	$\pm 3.0\%$	—	$\pm 3.0\%$
other acceptance syst.	—	$\pm 2.0\%$	$\pm 2.0\%$
non-W (rate)	$\pm 1.5\%$	—	$\pm 1.5\%$
$t\bar{t}$ shape	$\pm 1.5\%$	—	$\pm 1.5\%$
$t\bar{b}$ (single top production)	$\pm 0.5\%$	—	$\pm 0.5\%$
total	$^{+12.4\%}_{-13.9\%}$	$\pm 12.3\%$	$^{+20.6\%}_{-21.5\%}$

TABLE IV: The top mass dependence of the measured total $t\bar{t}$ cross section. The acceptance and the leading jet E_T shape depend on the top quark mass.

mass (GeV/c^2)	170	175	180
cross section (pb)	$6.4^{+1.6+1.3}_{-1.7-1.4}$	$6.0^{+1.5+1.2}_{-1.6-1.3}$	$5.6^{+1.4+1.1}_{-1.5-1.2}$

Acknowledgments

We thank the Fermilab staff and the technical staffs of the participating institutions for their vital contributions. This work was supported by the U.S. Department of Energy and National Science Foundation; the Italian Istituto Nazionale di Fisica Nucleare; the Ministry of Education, Culture, Sports, Science and Technology of Japan; the Natural Sciences and Engineering Research Council of Canada; the National Science Council of the Republic of China; the Swiss National Science Foundation; the A.P. Sloan Foundation; the Bundesministerium fuer Bildung und Forschung, Germany; the Korean Science and Engineering Foundation and the Korean Research Foundation; the Particle Physics and Astronomy Research Council and the Royal Society, UK; the Russian Foundation for Basic Research; the Comision Interministerial de Ciencia y Tecnologia, Spain; in part by the European Community's Human Potential Programme under contract HPRN-CT-2002-00292, Probe for New Physics; and by the Research Fund of Istanbul University Project No. 1755/21122001.

[1] CDF Collaboration, T. Affolder *et al.*, Phys. Rev. D **64**, 032002 (2001); D0 collaboration, V.M. Abazov *et al.*, Phys. Rev. D **67**, 012004 (2003).

[2] D. Acosta *et al.*, Phys. Rev. Lett. (to be published); CDF II Collaboration, FERMILAB-

PUB-04-051-E; hep-ex/0404036.

[3] We use a cylindrical coordinate system where θ is the polar angle to the proton beam from the event vertex, ϕ is the azimuthal angle about the beam axis, and pseudorapidity is defined $\eta = -\ln\tan(\theta/2)$. We define transverse energy as $E_T = E\sin\theta$ and transverse momentum as $p_T = p\sin\theta$ where E is energy measured in the calorimeter and p is momentum measured by the spectrometer. Missing transverse energy, $\not\!\!E_T$, is $-|\Sigma_i E_T^i n_i|$, where n_i is the unit vector in the azimuthal plane that points from the beamline to the ith calorimeter tower.

[4] G. Marchesini *et al.*, Comput. Phys. Commun. **67**, 465 (1992); G. Corcella *et al.*, J. High Energy Phys. **0101**, 010 (2001).

[5] T. Sjöstrand *et al.*, Comput. Phys. Commun. **135**, 238 (2001).

[6] M.L. Mangano *et al.*, J. High Energy Phys. **0307**, 001 (2003).

[7] CDF II collaboration, FERMILAB-PUB-96/390-E.

[8] CDF II collaboration, D. Acosta *et al.*, to be submitted to Phys. Rev. D.

[9] CDF II collaboration, D. Acosta *et al.*, to be submitted to Phys. Rev. D.

[10] J. Campbell and J. Huston, hep-ph/0405276 to be submitted to Phys. Rev. D.

[11] J.M. Campbell and R.K. Ellis, Phys. Rev. D **60**, 113006 (1999);

[12] The Top Averaging Group for the CDF and D0 collaborations, L. Demortier *et al.*, FERMILAB-TM-2084 (1999)

[13] B. Harris *et al.*, Phys. Rev. D **66**, 054024 (2002).

[14] R. Bonciani, S. Catani, M.L. Mangano, and P. Nason, Nucl. Phys. **B529**, 424 (1998); hep-ex/0303085.